CrystEngComm

ROYAL SOCIETY OF CHEMISTRY

PAPER

View Article Online
View Journal | View Issue

Cite this: *CrystEngComm*, 2021, **23**, 629

Fabrication of a dual-emitting RhB@Zn-1 composite as a recyclable luminescent sensor for sensitive detection of nitrofuran antibiotics†

Qian-Qian Tu,[a] Ling-Ling Ren,[a] Ai-Ling Cheng *[a] and En-Qing Gao [b]

Received 10th October 2020,
Accepted 23rd November 2020

DOI: 10.1039/d0ce01483d

rsc.li/crystengcomm

A novel 3D anionic porous metal–organic framework $\{[(CH_3)_2NH_2][Zn_3(\mu_3\text{-}OH)(L)_2(H_2O)]\cdot 4H_2O\cdot 3DMA\}_n$ (**Zn-1**) (H_2L = 1-hydroxy-5,5-dioxodibenzothiophen-3,7-dicarboxylic acid, DMA = dimethylacetamide) has been solvothermally synthesized. Single-crystal X-ray analyses reveal that the framework of **Zn-1** is based on deformed triangular $[Zn_3O]$ clusters with interlinked 1D channels. Taking advantage of the high porosity and charged skeleton of **Zn-1**, fluorescent dye rhodamine B (RhB) molecules can be successfully incorporated into the channels of **Zn-1** *via* an ion-exchange process. Due to the spatial confinement, the **RhB@Zn-1** composite shows dual-emission properties including the emissions of **Zn-1** centered at 475 nm and RhB centered at 580 nm. Moreover, **RhB@Zn-1** can be used as a recyclable fluorescent sensor for sensitive and selective detection of nitrofuran antibiotics (nitrofurantoin and nitrofurazone), with high K_{SV} values (5.61×10^4 M^{-1} and 4.73×10^4 M^{-1}) and low detection limits (0.73 μM and 0.86 μM). Comparison experiment results show that the sensing capability of **Zn-1** can be greatly improved *via* the dye-encapsulation strategy. Further studies reveal that the synergistic effect of competitive absorption and photo-induced electron transfer causes the fluorescence quenching of **Zn-1**, which in turn decreases the energy transfer from **Zn-1** to RhB and leads to the quenching process of RhB.

1. Introduction

Antibiotics, as an important class of pharmaceuticals, have been universally employed in treating bacterial infections.[1,2] However, the desperate use of antibiotics has resulted in high levels of antibiotic residues in the ecological environment. Owing to their potential toxicity and degradation difficulty, the antibiotic residues might pose serious threats to the health of humans and wildlife.[3,4] Particularly, they might not only cause antibiotic resistance and immunity decline, but also increase the risk of genetic defects and cancer.[5,6] Hence, it is quite urgent to explore reliable and high-efficiency methods for antibiotic residue detection. So far, the commercial detection methods mainly depend on technique-based instruments, including high performance liquid chromatography, Raman spectroscopy, capillary chromatography, *etc.*[7–9] However, these detection technologies are usually complicated, time-consuming and expensive. In contrast to the instrument-based methods, luminescence sensing is considered to be more promising because of its low cost, high sensitivity, short response time and simple operation.[10–12]

Metal–organic frameworks (MOFs), as a class of burgeoning porous hybrid crystalline materials, have shown potential applications in many fields due to their fascinating structures and superior physicochemical properties.[13–20] Among them, luminescent MOFs (LMOFs) can be easily constructed by the judicious selection of various inorganic or organic luminescent moieties. On account of their structural diversity, high porosity and tunable fluorescence properties, LMOFs have been widely exploited as unique chemical and biological sensors.[21–30] Moreover, fluorescent dye molecules or other fluorescent guests can be encapsulated into the pores of MOFs through the ion-exchange process and/or space confinement effect.[31,32] In fact, the aggregation-induced quenching (AIQ) effect of the fluorescent dye molecules can be avoided effectively by the dispersion effect of the uniform pores of MOFs. Therefore, dual-emitting or multi-emitting dye@MOF composites with tunable luminescence properties can be fabricated through loading different guest dyes or adjusting the loading content. In recent years, some dye@MOF composites with dual-emission properties have

[a] *College of Chemistry and Molecular Engineering, East China Normal University, Shanghai 200240, People's Republic of China. E-mail: alcheng@chem.ecnu.edu.cn*
[b] *Shanghai Key Laboratory of Green Chemistry and Chemical Processes, College of Chemistry and Molecular Engineering, East China Normal University, Shanghai 200062, People's Republic of China*

† Electronic supplementary information (ESI) available. CCDC 2035830. For ESI and crystallographic data in CIF or other electronic format see DOI: 10.1039/d0ce01483d

been synthesized and utilized as multiplexed or even ratiometric sensors in sensing the temperature, pH, inorganic ions and small organic molecules.[33–40] However, they are still in the nascent stage for antibiotic detection.[41]

Recently, some sulfone-functionalized MOFs have been synthesized with 5,5-dioxodibenzothiophen-3,7-dicarboxylic acid (H_2L') and/or its derivatives as the bridging ligands. Some of the complexes can serve as fluorescent sensors for inorganic ions, NACs and antibiotics.[23,42–46] Previous studies have shown that H_2L' might be a good luminescent chromophore for LMOFs owing to its rigid and large π-conjugated system. In this report, we predesigned another structurally similar organic ligand [H_2L = 1-hydroxy-5,5-dioxodibenzothiophen-3,7-dicarboxylic acid] by decorating H_2L' with hydroxyl groups for enhancing the host–guest interactions. With H_2L as the bridging ligand for the first time, a novel 3D anionic metal–organic framework (**Zn-1**) was synthesized successfully. In the framework of **Zn-1**, there exist two kinds of interlinked 1D channels. Subsequently, a **RhB@Zn-1** composite with dual-emission luminescence properties was fabricated through embedding fluorescent rhodamine B (RhB) molecules into the channels of **Zn-1** *via* an ion-exchange process. Additionally, the **RhB@Zn-1** composite can be used as a fluorescent sensor for sensitive and selective detection of nitrofuran (NF) antibiotics. Comparison experiment results indicate that the sensing properties were greatly improved after dye encapsulation.

2. Experimental

Materials and measurements

The ligand 6-hydroxy-2,2′-sulfone-4,4′-dicarboxylic acid (H_2L) was synthesized according to a literature method.[47] The other reagents and solvents were commercially available and used directly without any further purification. The detailed description of the physical measurements and X-ray crystallographic analysis is shown in the ESI.† The crystal data and structure refinement for **Zn-1** are listed in Table S1.† CCDC no.: 2035830.

Synthesis of $\{[(CH_3)_2NH_2][Zn_3(\mu_3\text{-}OH)(L)_2(H_2O)]\cdot 4H_2O\cdot 3DMA\}_n$ (Zn-1). Complex **Zn-1** was prepared using a solvothermal method. Typically, a mixture of $Zn(NO_3)_2\cdot 6H_2O$ (30 mg, 0.10 mmol), H_2L (20 mg, 0.06 mmol) and 4,4′-bipyridine (4,4′-bipy, 15.6 mg, 0.1 mmol) was dissolved in a solution of dimethylacetamide (DMA, 8 mL) and H_2O (0.2 ml). The mixture was sealed in a 23 mL Teflon-lined reactor and heated at 373 K for 5 days. Pale-yellow hexagonal prism shaped crystals were obtained after cooling to room temperature. Yield of 70% (based on H_2L). Anal. calcd. (%) for $Zn_3C_{42}H_{56}O_{23}N_4S_2$: C 40.5, H 4.53, N 4.50. Found: C 39.28 H 4.90, N 4.21. IR (KBr pellet, cm^{-1}): 3230w, 1620s, 1540w, 1380s, 1380s, 1300m, 1260m, 1140w, 1020w, 889m, 793m, 760w, 700m, 621m, 469w.

Synthesis of RhB@Zn-1. The powder of **Zn-1** (100 mg) was immersed in 80 ml DMA solution of RhB (0.1 mM) and kept for three days at room temperature. The color of the powder changed gradually from pale yellow to orange, while the color of the RhB solution faded into nearly colorless. The ion exchange process was monitored simultaneously by UV-vis spectroscopy. Afterwards, the orange samples of **RhB@Zn-1** were separated and washed thoroughly with DMA and ethanol. The activated samples were obtained by drying the as-synthesized samples at 50 °C under vacuum for 6 h.

3. Results and discussion

Synthesis and structure description

Zn-1 has been synthesized by the solvothermal reaction of $Zn(NO_3)_2\cdot 6H_2O$ with H_2L in DMA/H_2O mixed solutions with 4,4′-bipy as the template. X-ray single-crystal diffraction analysis reveals that **Zn-1** features a 3D anionic framework based on deformed trinuclear clusters. It crystallizes in an orthorhombic system with the space group *Pnma*. The asymmetric unit of **Zn-1** contains half a $\{[(CH_3)_2NH_2][Zn_3(\mu_3\text{-}OH)(L)_2(H_2O)]\cdot 4H_2O\cdot 3DMA\}_n$ molecule. In each cluster, there exist two kinds of coordination modes for the Zn atoms. The Zn1 atom is surrounded by one μ_3-OH oxygen atom, four carboxylate oxygen atoms from four different L^{2-} ligands and one water oxygen atom [Zn–O bond lengths: 2.050(2)–2.2069(18) Å, O–Zn–O angles: 81.43(13)–95.35(6)°], generating a slightly distorted $\{ZnO_6\}$ octahedral geometry. The Zn2 atom is coordinated by one μ_3-OH oxygen atom, two carboxylate oxygen atoms from two independent L^{2-} ligands and one hydroxyl O atom from another L^{2-} ligand, showing a distorted tetrahedral geometry [Zn–O bond lengths: 1.9071(13)–1.9852(6) Å, O–Zn–O angles: 101.72(6)–118.48(7)°]. Furthermore, three Zn ions are joined by one μ_3-OH to generate a deformed $[Zn_3O]$ cluster, with the Zn⋯Zn distances in the range of 3.2225(0)–3.7768(0) Å and the Zn–O–Zn angles in the range of 100.63–143.89°. Notably, the clusters in **Zn-1** are different from the well-known $[M_3O/M_3OH]$ clusters in MIL-101.[48] In each cluster of the MIL-101 series, three metal atoms form an ideal triangle around μ_3-O. There are two μ_2-carboxylate bridges on each edge of the M_3O triangle, forming a 6-connected regular tri-prism SBU. Differently, in each Zn_3O cluster of **Zn-1**, there are two μ_2-carboxylate groups on each edge of the two edges (Zn1⋯Zn2 and Zn1A⋯Zn2), but no carboxylate bridge is involved in the remaining one edge (Zn1⋯Zn1A). Besides, one vertex of the triangle is ligated by one terminal H_2O molecule. As for the other two vertices, each is occupied by one hydroxyl group. As a result, each Zn_3O cluster is furnished by four carboxylate groups, two hydroxyl groups and one H_2O molecule, forming a 6-connected irregular tri-prism SBU (Fig. 1a). Remarkably, the cluster of **Zn-1** is similar to the Ga_3O cluster of **SNNU-63**.[49] The difference is that each hydroxyl group is replaced by one chelated carboxylate group in the Ga_3O cluster, and the edge of Ga1⋯Ga1A is bridged by a terminal acetate group.

Similar to the structure of **SNNU-63**, adjacent trinuclear clusters in **Zn-1** are connected by double L^{2-} bridges *via* the carboxylate and hydroxyl groups, forming a zigzag chain along the *b* direction (Fig. 1d). Then each zigzag chain is

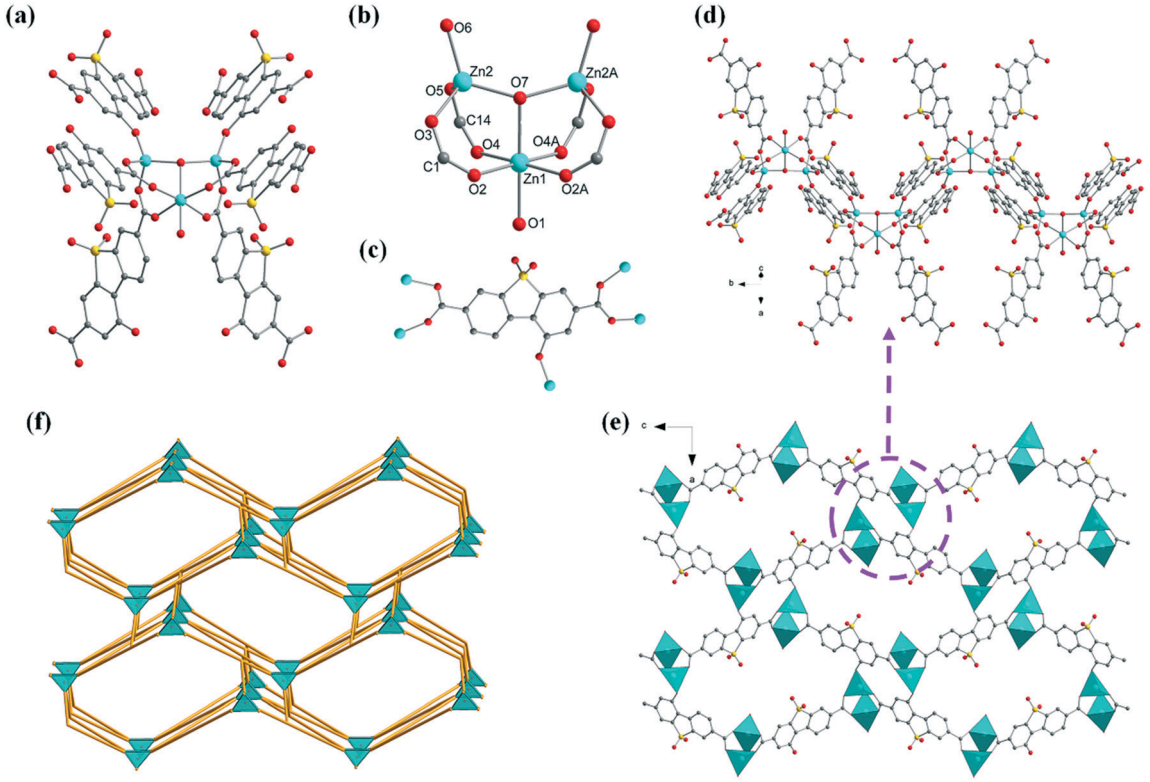

Fig. 1 Molecular structure of **Zn-1**: (a) the building unit; (b) the trinuclear $[Zn_3(\mu_3\text{-}OH)(COO)_4(O)_2(H_2O)]$ cluster; (c) the coordination environment of the H_2L ligand; (d) 1D zigzag chain along the *b* axis; (e) three dimensional structure with 1D channels viewed along the *b* direction; (f) schematic depiction of the (6,3)-coordinated 3D network.

further connected to four neighboring chains by the L^{2-} ligands, leading to a three-dimensional anionic framework with two types of interlinked 1D channels: along the *a* direction: 10.86 × 18.44 Å^2, and along the *b* direction: 11.27 × 20.80 Å^2 (Fig. 1e and S3†). According to the PLATON[50] calculations, the total void value of the channels of **Zn-1** is about 66.6% of the crystal volume (4695.2 Å^3 out of the 7052.5 Å^3 unit cell volume). Enclosed in the channels are disordered guest molecules and $[(CH_3)_2NH_2]^+$ cations. Notably, $[(CH_3)_2NH_2]^+$ cations are generated *in situ* from the decomposition of DMA, and balance the negative charges of the framework.[51,52] To verify the $[(CH_3)_2NH_2]^+$ cations in the channel, 20 mg of **Zn-1** is immersed in NaCl D_2O solution (1.5 mL) for 48 h for the ion-exchange experiment, and then the supernatant is measured by ^1H NMR. As shown in Fig. S4,† a peak at 3.07 ppm belonging to the methyl group of the $[(CH_3)_2NH_2]^+$ cation is observed. Combining the charge balance considerations, elemental analyses and TG curve, the chemical formula of **Zn-1** is determined as $\{[(CH_3)_2NH_2][Zn_3(\mu_3\text{-}OH)(L)_2(H_2O)]\cdot 4H_2O \cdot 3DMA\}_n$.

From a topological viewpoint, the trinuclear cluster and the L^{2-} ligand can be considered as 6- and 3-connected nodes, respectively. As a result, the 3D framework of **Zn-1** can be simplified as a 6,3-connected 2-nodal network with a point symbol of $\{4^2\cdot 6\}_2\{4^4\cdot 6^2\cdot 8^9\}$, determined using the TOPOS program (Fig. 1f).[53]

Powder XRD and thermal analyses. The PXRD pattern of the as-synthesized sample of **Zn-1** is in good agreement with the simulated pattern, implying that the phase of the bulk products is pure (Fig. 2b). Thermogravimetric analysis (TGA) was carried out to evaluate the thermal stability of the framework of **Zn-1**. As shown in Fig. S5,† the TG curve of **Zn-1** shows a weight loss of 31.0% before 260 °C, owing to the loss of three DMA, four H_2O, one coordinated H_2O and one $[(CH_3)_2NH_2]^+$ (cal. 31.9%). Then, the main framework begins to decompose at about 350 °C.

On account of the high porosity and anionic framework of complex **Zn-1**, **Zn-1** can serve as a perfect host platform for construction of a dye@MOF composite by loading fluorescent cation dyes *via* the ion-exchange approach. RhB was chosen as the guest molecule due to the following facts: (1) the anionic framework of **Zn-1** could adsorb RhB cations *via* the ion-exchange process; (2) the window size of **Zn-1** (11.27 × 20.80 Å^2) is larger than the kinetic size of RhB (15.9 × 11.8 × 5.6 Å^3), therefore, RhB could enter the pores of **Zn-1**. Although RhB is an excellent fluorophore for chemical and biochemical sensing, its utilization is limited by the aggregation-induced quenching. Herein, RhB molecules can be encapsulated and isolated into the channels of **RhB@Zn-1** to avoid the occurrence of AIQ. After encapsulation, the color of the powder samples of **Zn-1** turns from pale yellow to orange under sunlight, and the luminescent color of the **Zn-1** suspension in EtOH turns from blue to yellow under UV light

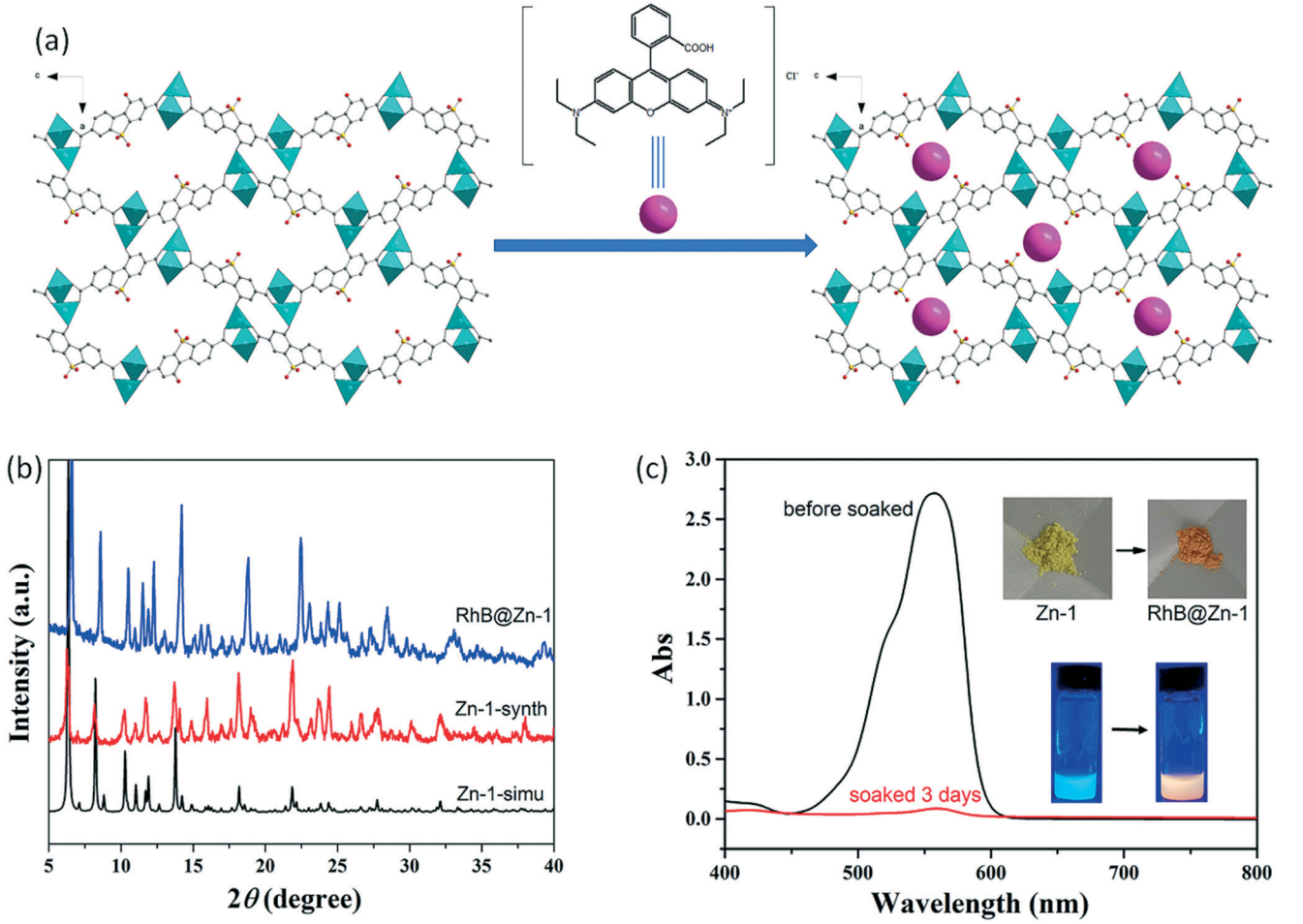

Fig. 2 (a) Three-dimensional (3D) frameworks of **Zn-1** and **RhB@Zn-1**; (b) the PXRD patterns of the simulated and prepared **Zn-1** and **RhB@Zn-1**; (c) UV-vis absorption spectra of the initial dye solution (black) and the supernatant after dye loading (red). The inset photographs show the color change of the powder samples of **Zn-1** under sunlight and the suspensions of **Zn-1** under a UV-vis lamp after dye loading.

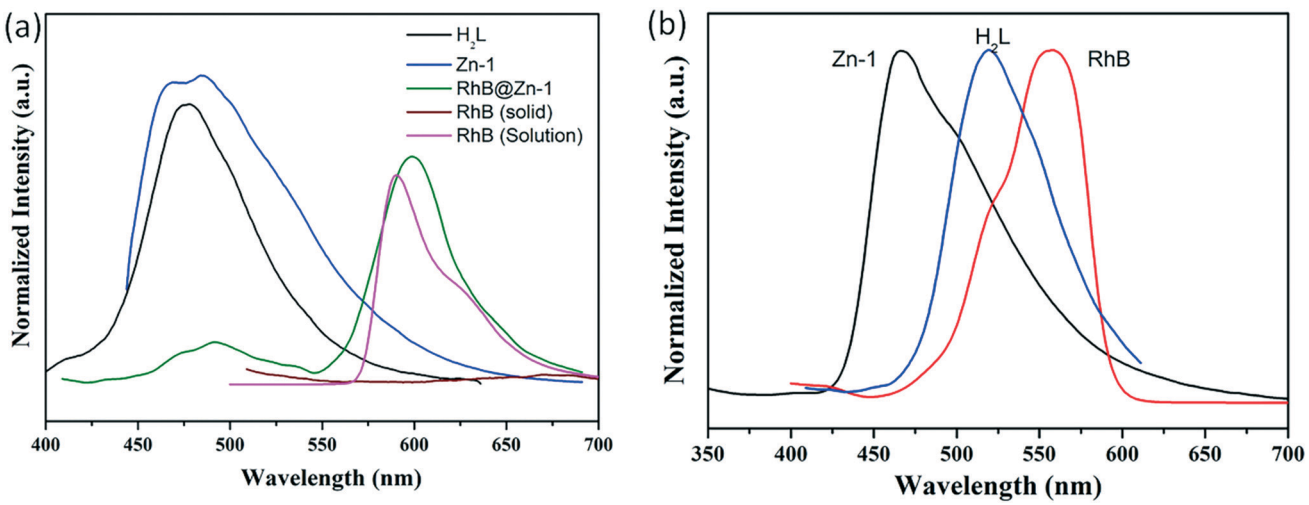

Fig. 3 (a) Fluorescence spectra of H_2L, **Zn-1**, **RhB@Zn-1**, RhB in the solid state, and RhB in EtOH solution (0.1 mmol); (b) normalized emission spectra of **Zn-1** (dispersed in EtOH) and H_2L (in EtOH) and UV-vis absorption spectrum of RhB in EtOH solution (0.1 mmol).

of 365 nm (Fig. 2c, inset pictures). Moreover, the XRD pattern of **RhB@Zn-1** is basically consistent with that of **Zn-1**, some of the peaks show a slight shift due to the encapsulation of the RhB molecules (Fig. 2b). Simultaneously, the ion-exchange process between RhB and $[(CH_3)_2NH_2]^+$ has been monitored by UV-vis spectroscopy. As depicted in Fig. 2c, after soaking for three days, the absorption band intensity of the RhB solution decreases significantly, and the ratio of loaded RhB on the **Zn-1** MOF is calculated to be about 3.4%. The above results show that RhB molecules have been loaded into the channels of **Zn-1** without destroying its crystal structure.

Fluorescence properties of Zn-1 and RhB@Zn-1. The solid-state luminescence emission spectra of H_2L, **Zn-1** and **RhB@Zn-1** as well as the excitation spectrum of **Zn-1** were measured at room temperature (Fig. 3a and S6†). Similar to that of H_2L, **Zn-1** shows a blue emission band centred at 475 nm upon excitation at 430 nm, suggesting that the emission of **Zn-1** originates from the H_2L ligand. As expected, RhB displays no emission in the solid state owing to the AIQ effect, whereas its EtOH solution shows a concentration-dependent yellow-orange emission at around 570–600 nm (Fig. S7†). As for **RhB@Zn-1**, the solid-state emission spectrum exhibits dual-emission luminescence properties (λ_{ex} = 430 nm), displaying a weak emission at 475 nm and a strong emission at 599 nm. Hence, the blue emission may originate from **Zn-1** while the orange emission may be attributed to RhB molecules. The above result further confirms that RhB molecules have been uniformly dispersed in the channels of **Zn-1**, thus inhibiting the occurrence of AIQ. Notably, the distance of the two emission peaks is as large as 125 nm and nearly without overlap, suggesting that the interference between the two emission bands can be avoided. Moreover, the fluorescence intensity at 599 nm is almost 5 times higher than that at 475 nm, which shows that the fluorescence of the composite is mainly dominated by the emission of loaded RhB molecules. In addition, the UV-vis spectrum of the RhB solution exhibits an absorption band centered at 545 nm, which has partial spectral overlap with the emission peak of **Zn-1** (Fig. 3b). The result illustrates the presence of fluorescence resonance energy transfer (FRET) from **Zn-1** to RhB molecules.[40] This is also confirmed by the decreased emission at 475 nm in **RhB@Zn-1** along with the increase of the loading amount of RhB. Based on the ligand based emission properties of **Zn-1**, the energy transfer process between H_2L and RhB is also investigated (Fig. 3b and S8†). As expected, partial spectral overlap is observed between the emission of H_2L and the absorption band of RhB. Moreover, the emission intensity of the EtOH solution of H_2L decreases gradually with the increase of RhB. The results confirm that resonance energy can be transferred from H_2L to RhB. When the ground powder of **RhB@Zn-1** is dispersed in EtOH, the emission derived from loaded RhB shifts slightly from 599 nm to 585 nm owing to the solvation effect (λ_{ex} = 360 nm). Additionally, the emission intensity of the suspension remains almost unchanged for at least 70 min, which demonstrates the high luminescence stability of the composite (Fig. S9a†).

Detection of antibiotics. On account of the excellent luminescence and good stability of composite **RhB@Zn-1** in EtOH, the luminescence sensing ability of the composite for selective detection of antibiotics was explored. Five commonly used antibiotics have been selected as the analytes: nitrofurantoin (NFT), nitrofurazone (NZF), metronidazole (MDZ), sulfadiazine (SDZ) and thiamphenicol (THI) (Fig. S10†). Firstly, finely ground samples of **RhB@Zn-1** (3 mg) were immersed in 5.00 mL of EtOH and sonicated for 30 min. Then, the luminescence spectra of **RhB@Zn-1** were recorded upon addition of 600 μM antibiotics. Obviously, these antibiotics cause different degrees of fluorescence quenching, a slight or negligible fluorescence decrease occurs upon addition of THI, MDZ or SDZ; however, NFT and NZF both result in a significant quenching effect. Totally, the quenching order for the above antibiotics is NFT, NZF > MDZ > THI, SDZ (Fig. 4). The results suggest that **RhB@Zn-1** can be a potential luminescence sensor for selective sensing of NF antibiotics. To further evaluate the sensitivity of **RhB@Zn-1** for NFT or NZF, the fluorescence quenching process was investigated by gradually adding NFT or NZF into the suspension of **RhB@Zn-1**. As can be seen, dual-emission peaks of **RhB@Zn-1** both quenched steadily with a gradual increase of NFT or NZF (Fig. 5a and c). Here, the fluorescence band at 585 nm was selected as the detection signal due to its strong emission. Particularly, the quenching efficiencies can reach 14.4% and 13.3% for NFT and NZF upon adding only 10 μM antibiotics. Upon addition of 420 μM antibiotics, the quenching efficiencies increase rapidly to 94.7% and 93.1% for NFT and NZF, respectively. Remarkably, the luminescence intensity can be completely quenched within 1 min, implying the fast response of **RhB@Zn-1** towards NFT and NZF (Fig. S9b†). Moreover, the **RhB@Zn-1** suspension shows concentration-dependent fluorescent colors with incremental addition of NFT, which can be observed obviously under a UV lamp (Fig. S11†). In addition, the

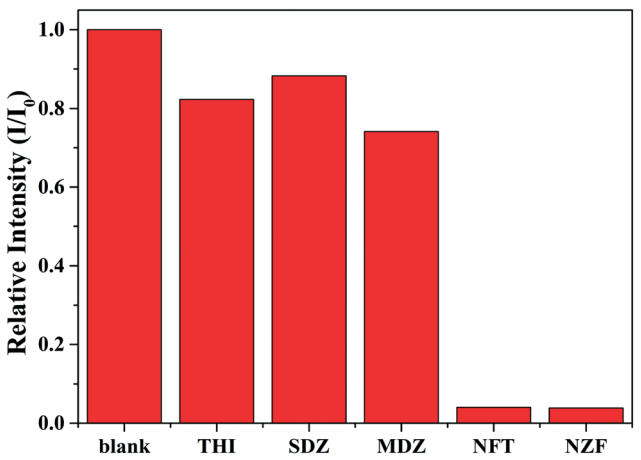

Fig. 4 The luminescence intensities at 575 nm (λ_{ex} = 360 nm) of **RhB@Zn-1** dispersed in EtOH containing various antibiotics (600 μM).

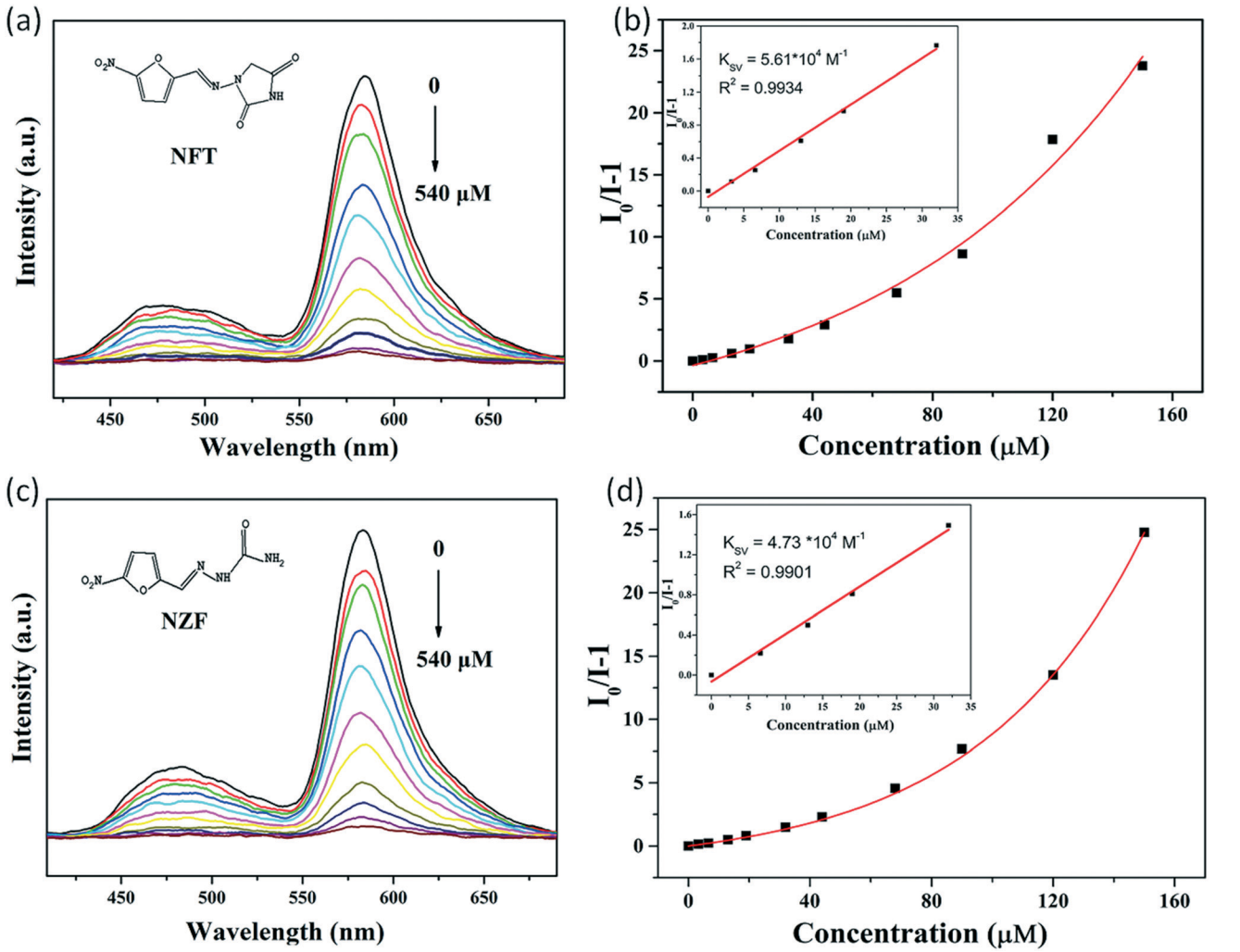

Fig. 5 Emission spectra of **RhB@Zn-1** upon incremental addition of NFT (a) and NFZ (c); the Stern–Volmer plots of **RhB@Zn-1** for NFT (b) and NFZ (d). Inset: Linear relationship of the SV plots at low concentration.

luminescence quenching effect can be quantitatively analyzed by the Stern–Volmer (SV) equation: $I_0/I = K_{SV}[A] + 1$, where K_{SV} is the quenching constant (M^{-1}), $[A]$ is the molar concentration of the nitrofuran antibiotics (mol L^{-1}), and I_0 and I are the luminescence intensities at 585 nm in the absence and presence of the analytes. The SV plots for both of NFT and NZF are nearly linear at the low concentration range but bend upward at higher concentrations (Fig. 5b and d), which might be due to a resonant energy-transfer (RET) process and/or the coexistence of dynamic and static quenching processes.[54,55] According to the linear part of the SV plots, the K_{SV} values for NFT and NZF are estimated to be 5.61×10^4 M^{-1} and 4.73×10^4 M^{-1}, respectively. Further, the LOD values for NFT and NZF are calculated to be 0.73 μM and 0.86 μM using equation $3\sigma/K$ (σ denotes the standard deviation of the blank solution and K signifies the slope of the emission intensity *vs.* analyte concentration plot). Remarkably, the observed K_{SV} and LOD values are superior to those reported values of other luminescent MOFs.[24,30,56–58] The large K_{SV} values and small LOD values indicate that **RhB@Zn-1** can serve as a promising sensor for the sensitive and selective detection of NFT or NFZ. Meanwhile, the sensing ability of **Zn-1** towards NFT or NZF was also investigated and the results are shown in Fig. S12 and S13 and Table S1.† By comparing, it can be found that the sensing properties can be greatly improved after dye encapsulation. The above analyses reveal that the fluorescence sensing ability of **Zn-1** toward NF antibiotics can be improved *via* a dye-incorporation strategy. On account of the ligand-based luminescence of **Zn-1**, the sensing ability of the H_2L ligand is also studied. The results show that the emission of the H_2L ligand in EtOH also shows a certain extent of quenching upon adding NFT in the absence or presence of RhB (Fig. S14 and S15†).

To evaluate the selectivity of the **RhB@Zn-1** composite towards NFT or NFZ, the anti-interference performance was explored in the presence of other interfering antibiotics (THI, SDZ and MDZ). As shown in Fig. S16,† upon the addition of NFT or NZF into the suspensions containing equimolar amounts of other interfering antibiotics, a significant

quenching still occurs rapidly. The results illustrate that the sensing processes are not interfered by the coexistence of the above interfering antibiotics. Additionally, the recycling experiments of **RhB@Zn-1** for sensing NFT or NZF were investigated. The powder of **RhB@Zn-1** can be easily recollected by centrifugation and washing with EtOH. As can be seen from Fig. S17,† after being recycled four times, the fluorescence intensities of **RhB@Zn-1** remain unchanged for NZF but decrease by about 17% for NFT. We speculate that the intensity decay of **RhB@Zn-1** for NFT might be caused by the adsorption effect. To test this, the changes of the absorption peak intensity of the NFT or NZF solution before and after adding **RhB@Zn-1** have been measured. As shown in Fig. S18,† the absorption intensity of NFT decreases to some extent after adding **RhB@Zn-1**, however, the intensity of NZF remains unchanged. The results indicate that a small amount of NFT molecules can be adsorbed onto the framework of **RhB@Zn-1** during the sensing process, thus leading to a certain extent of irreversible decay of the fluorescence intensity. Besides, the XRD patterns of the regenerated samples of **RhB@Zn-1** are basically identical to those of the original samples, implying that the skeleton remains unchanged during the sensing experiments (Fig. S19†). These results illustrate that **RhB@Zn-1** has good recyclability and stability for the detection of NF antibiotics in EtOH, especially for NZF.

Mechanism of RhB@Zn-1 towards antibiotics. It is significant to explore the possible quenching mechanisms of **RhB@Zn-1** by NFT or NZF. Firstly, the PXRD patterns of **RhB@Zn-1** after detection experiments are basically identical to the simulated samples, implying that the quenching effect is not ascribed to the collapse of the framework (Fig. S19†). Secondly, the quick response and easy recycling of the composite for NZF suggests that the quenching is also not caused by the adsorption of the guest molecules. As for NFT, the quenching has a certain relationship with guest adsorption. Then, the UV-vis absorption spectra of the selected antibiotics have been measured (Fig. 6). The absorption bands of the analytes have no overlap with the excitation/emission spectra of RhB and the emission spectrum of H_2L, **Zn-1** or **RhB@Zn-1**, which shows that: (1) competitive absorption or FRET does not occur between the analytes and RhB; (2) no FRET process occurs between the analytes and H_2L, **Zn-1** or **RhB@Zn-1**. On the other hand, the spectra of NFT and NZF both have large overlaps with the excitation spectrum (λ_{ex} = 360 nm) of H_2L, **Zn-1** or **RhB@Zn-1**. However, MDZ just shows a minor overlap, while THI or SDZ has no overlap with the excitation band. Generally, the overlap extent is usually proportional to the contribution of the competitive absorption of the excitation energy between the sensors and the analytes. As a result, the competitive absorption causes the emission quenching of **Zn-1**, which in turn decreases the energy transfer from the ligand of **Zn-1** to RhB and causes a quenching effect of RhB.[37,40] As can be seen, the order of quenching efficiencies of **RhB@Zn-1** towards the selected antibiotics is basically in accordance with the extent of the spectral overlap, which indicates that the quenching process towards NFT or NZF is related to the competitive absorption.

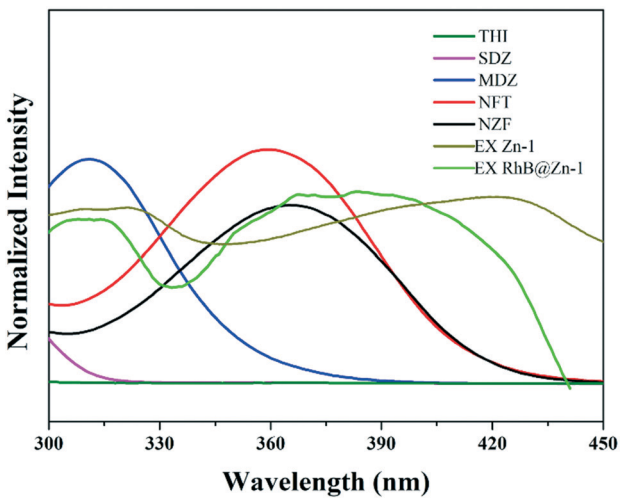

Fig. 6 Spectral overlap between the absorption spectra of various antibiotics and the excitation spectrum of **RhB@Zn-1**.

On the other hand, in view of the electron sufficient nature of the ligand of **Zn-1** and the electron deficient nature of the nitro group of NF antibiotics, the photo-induced electron transfer (PET) mechanism is also proposed. In general, the excited electrons from ligands can be transferred to the lowest unoccupied molecular orbital (LUMO) of the analytes, resulting in a fluorescence quenching effect. Similarly, PET may also decrease the energy transfer from the ligand of **Zn-1** to RhB and result in the quenching effect of RhB. The lower the LUMO energy of the analytes, the more easily the electrons are transferred to the acceptor. To verify this, the highest occupied molecular orbital (HOMO) and LUMO energy levels of the above analytes are calculated based on the density functional theory (DFT) method. As shown in Fig. S20,† the LUMO energy levels of the antibiotics are in the order NFT, NZF < MDZ < THI < SDZ, which illustrates the highly selective and sensitive sensing performance of **RhB@Zn-1** for NFT or NZF. Based on the above analysis, we speculate that the synergetic effect of competitive absorption and photo-induced electron transfer leads to the quenching of **Zn-1**, which in turn decreases the energy transfer from **Zn-1** to RhB and results in the quenching process of RhB.

4. Conclusion

In summary, a novel 3D anionic metal–organic framework (**Zn-1**) has been synthesized, which is based on triangular trinuclear clusters with large interlinked 1D channels. By virtue of the high porosity and charged skeleton of **Zn-1**, a dual-emission **RhB@Zn-1** composite was fabricated by encapsulating RhB dye molecules into the channels *via* the ion-exchange process. Moreover, the composite can serve as a recyclable sensor for sensitive and selective detection of NFT

or NZF *via* the luminescence quenching process, with high K_{SV} values and low LODs. It was found that the sensing ability of **Zn-1** can be greatly improved after dye encapsulation. Further studies reveal that the synergetic effect of competitive absorption and the PET mechanism may not only cause the quenching process of **Zn-1** but also decrease the energy transfer from **Zn-1** to RhB and lead to the quenching effect of RhB.

Conflicts of interest

There are no conflicts to declare.

Acknowledgements

This work is financially supported by the National Natural Science Foundation of China (Grant No. 21971069).

References

1 J. L. Martinez, *Environ. Pollut.*, 2009, **157**, 2893–2902.
2 S. Rodriguez-Mozaz, S. Chamorro, E. Marti, B. Huerta, M. Gros, A. Sanchez-Melsio, C. M. Borrego, D. Barcelo and J. Luis Balcazar, *Water Res.*, 2015, **69**, 234–242.
3 X. Liu, J. C. Steele and X. Z. Meng, *Environ. Pollut.*, 2017, **223**, 161–169.
4 M. L. Han, G. X. Wen, W. W. Dong, Z. H. Zhou, Y. P. Wu, J. Zhao, D. S. Li, L. F. Ma and X. H. Bu, *J. Mater. Chem. C*, 2017, **5**, 8469–8474.
5 H. T. Bai, H. X. Yuan, C. Y. Nie, B. Wang, F. T. Lv, L. B. Liu and S. Wang, *Angew. Chem., Int. Ed.*, 2015, **54**, 13208–13213.
6 K. Kummerer, *Chemosphere*, 2009, **75**, 417–434.
7 Y. T. Li, L. L. Qu, D. W. Li, Q. X. Song, F. Fathi and Y. T. Long, *Biosens. Bioelectron.*, 2013, **43**, 94–100.
8 C. Blasco, A. Di Corcia and Y. Pico, *Food Chem.*, 2009, **116**, 1005–1012.
9 M. Gao, J. Wang, X. K. Song, X. He, R. A. Dahlgren, Z. Z. Zhang, S. G. Ru and X. D. Wang, *Anal. Bioanal. Chem.*, 2018, **410**, 2671–2687.
10 F. Zhang, H. Yao, Y. F. Zhao, X. Li, G. W. Zhang and Y. Y. Yang, *Talanta*, 2017, **174**, 660–666.
11 K. Ngamdee, T. Tuntulani and W. Ngeontae, *Sens. Actuators, B*, 2015, **216**, 150–158.
12 Y. Feng, D. Y. Deng, L. C. Zhang, R. Liu and Y. Lv, *Sens. Actuators, B*, 2019, **279**, 189–196.
13 A. Dhakshinamoorthy, A. M. Asiri and H. Garcia, *Adv. Mater.*, 2019, **31**, 1900617.
14 A. Karmakar and A. J. L. Pombeiro, *Coord. Chem. Rev.*, 2019, **395**, 86–129.
15 L. Li, J. He, Y. Wang, X. Lv, X. Gu, P. Dai, D. Liu and X. Zhao, *J. Mater. Chem. A*, 2019, **7**, 1964–1988.
16 H.-S. Wang, *Coord. Chem. Rev.*, 2017, **349**, 139–155.
17 B. Zhang and L. Sun, *Chem. Soc. Rev.*, 2019, **48**, 2216–2264.
18 Y. Zhang, S. Yuan, G. Day, X. Wang, X. Yang and H.-C. Zhou, *Coord. Chem. Rev.*, 2018, **354**, 28–45.
19 W. Zhu, J. Zhao, Q. Chen and Z. Liu, *Coord. Chem. Rev.*, 2019, **398**, 113009.
20 T. Rasheed and F. Nabeel, *Coord. Chem. Rev.*, 2019, **401**, 213065.
21 T. Gong, P. Li, Q. Sui, J. Chen, J. Xu and E.-Q. Gao, *J. Mater. Chem. A*, 2018, **6**, 9236–9244.
22 R. Goswami, S. C. Mandal, N. Seal, B. Pathak and S. Neogi, *J. Mater. Chem. A*, 2019, **7**, 19471–19484.
23 H. He, Q.-Q. Zhu, C.-P. Li and M. Du, *Cryst. Growth Des.*, 2018, **19**, 694–703.
24 H. He, Q.-Q. Zhu, F. Sun and G. Zhu, *Cryst. Growth Des.*, 2018, **18**, 5573–5581.
25 J.-M. Li, R. Li and X. Li, *CrystEngComm*, 2018, **20**, 4962–4972.
26 P. Li, X.-M. Yin, L.-L. Gao, S.-L. Yang, Q. Sui, T. Gong and E.-Q. Gao, *ACS Appl. Mater. Interfaces*, 2019, **2**, 4646–4654.
27 J. Sun, P. Guo, M. Liu and H. Li, *J. Mater. Chem. A*, 2019, **7**, 8992–8999.
28 C. Xu, C. Bi, Z. Zhu, R. Luo, X. Zhang, D. Zhang, C. Fan, L. Cui and Y. Fan, *CrystEngComm*, 2019, **21**, 2333–2344.
29 N. Xu, Q. Zhang and G. Zhang, *Dalton Trans.*, 2019, **48**, 2683–2691.
30 Y. Zhao, Y.-J. Wang, N. Wang, P. Zheng, H.-R. Fu, M.-L. Han, L.-F. Ma and L.-Y. Wang, *Inorg. Chem.*, 2019, **58**, 12700–12706.
31 H.-R. Fu, X.-X. Wu, L.-F. Ma, F. Wang and J. Zhang, *ACS Appl. Mater. Interfaces*, 2018, **10**, 18012–18020.
32 S. Wu, H. Min, W. Shi and P. Cheng, *Adv. Mater.*, 2019, **32**, 1805871.
33 H.-R. Fu, L.-B. Yan, N.-T. Wu, L.-F. Ma and S.-Q. Zang, *J. Mater. Chem. A*, 2018, **6**, 9183–9191.
34 Y. Li, Z. Wei, Y. Zhang, Z. Guo, D. Chen, P. Jia, P. Chen and H. Xing, *ACS Sustainable Chem. Eng.*, 2019, **7**, 6196–6203.
35 W. Liu, C. Chen, X. Huang, E. Xie and W. Liu, *Chem. – Eur. J.*, 2019, **25**, 10054–10058.
36 Z. Sun, Y. Ling, S. G. Liu, Y. Z. Yang, X. H. Wang, Y. Z. Fan, N. B. Li and H. Q. Luo, *Inorg. Chem.*, 2019, **58**, 8388–8395.
37 Z. Wei, D. Chen, Z. Guo, P. Jia and H. Xing, *Inorg. Chem.*, 2020, **59**, 5386–5393.
38 J. Zhang, W. Zhou, L. Zhai, X. Niu and T. Hu, *CrystEngComm*, 2020, **22**, 1050–1056.
39 N. Zhang, D. Zhang, J. Zhao and Z. Xia, *Dalton Trans.*, 2019, **48**, 6794–6799.
40 Z. Zhang, Z. Wei, F. Meng, J. Su, D. Chen, Z. Guo and H. Xing, *Chem. – Eur. J.*, 2020, **26**, 1661–1667.
41 M. Yu, Y. Xie, X. Wang, Y. Li and G. Li, *ACS Appl. Mater. Interfaces*, 2019, **11**, 21201–21210.
42 J.-L. Gu, X.-W. Tao, Q.-Q. Tu, A.-L. Cheng and E.-Q. Gao, *J. Solid State Chem.*, 2020, **286**, 121318.
43 L.-L. Ren, Y.-Y. Cui, A.-L. Cheng and E.-Q. Gao, *J. Solid State Chem.*, 2019, **270**, 463–469.
44 Q.-Q. Tu, L.-L. Ren, Y.-Y. Cui, A.-L. Cheng and E.-Q. Gao, *CrystEngComm*, 2020, **22**, 1789–1801.
45 S. Xiong, S. Wang, X. Tang and Z. Wang, *CrystEngComm*, 2011, **13**, 1646–1653.
46 L. Yan, Q. Yue, Q.-X. Jia, G. Lemercier and E.-Q. Gao, *Cryst. Growth Des.*, 2009, **9**, 2984–2987.
47 V. K. Olkhovik, D. A. Vasilevskii, A. A. Pap, G. V. Kalechyts, Y. V. Matveienko, A. G. Baran, N. A. Halinouski and V. G. Petushok, *ARKIVOC*, 2008, 69–93.

48 O. I. Lebedev, F. Millange, C. Serre, G. Van Tendeloo and G. Ferey, *Chem. Mater.*, 2005, **17**, 6525–6527.
49 Y. T. Li, J. W. Zhang, H. J. Lv, M. C. Hu, S. N. Li, Y. C. Jiang and Q. G. Zhai, *Inorg. Chem.*, 2020, **59**, 10368–10373.
50 A. L. Spek, *J. Appl. Crystallogr.*, 2003, **36**, 7–13.
51 W. Du, Z. Zhu, Y.-L. Bai, Z. Yang, S. Zhu, J. Xu, Z. Xie and J. Fang, *Chem. Commun.*, 2018, **54**, 5972–5975.
52 Z. Cui, X. Zhang, S. Liu, L. Zhou, W. Li and J. Zhang, *Inorg. Chem.*, 2018, **57**, 11463–11473.
53 V. A. Blatov, L. Carlucci, G. Ciani and D. M. Proserpio, *CrystEngComm*, 2004, **6**, 377–395.
54 S. S. Nagarkar, A. V. Desai and S. K. Ghosh, *Chem. Commun.*, 2014, **50**, 8915–8918.
55 H. Sohn, M. J. Sailor, D. Magde and W. C. Trogler, *J. Am. Chem. Soc.*, 2003, **125**, 3821–3830.
56 D. Zhao, X.-H. Liu, Y. Zhao, P. Wang, Y. Liu, M. Azam, S. I. Al-Resayes, Y. Lu and W.-Y. Sun, *J. Mater. Chem. A*, 2017, **5**, 15797–15807.
57 Z.-W. Zhai, S.-H. Yang, M. Cao, L.-K. Li, C.-X. Du and S.-Q. Zang, *Cryst. Growth Des.*, 2018, **18**, 7173–7182.
58 Q.-Q. Zhu, H. He, Y. Yan, J. Yuan, D.-Q. Lu, D.-Y. Zhang, F. Sun and G. Zhu, *Inorg. Chem.*, 2019, **58**, 7746–7753.